A hydrophobic core in the coiled-coil domain essential for NRC resistosome function

Hung-Yu Wang[1,2,3], Kim-Teng Lee[1,2,3], Foong-Jing Goh[1,2,3], Tolga O. Bozkurt[4], Chih-Hang Wu[1,2,5]*

[1] Institute of Plant and Microbial Biology, Academia Sinica, Taipei 115201, Taiwan
[2] Molecular and Biological Agricultural Sciences Program, Taiwan International Graduate Program, National Chung-Hsing University and Academia Sinica, Taipei 115201, Taiwan
[3] Graduate Institute of Biotechnology, National Chung-Hsing University, Taichung 402202, Taiwan
[4] Department of Life Sciences, Imperial College London, London SW7 2AZ, UK
[5] Biotechnology Center, National Chung-Hsing University, Taichung 402202, Taiwan

*Correspondence to wuchh@gate.sinica.edu.tw

Abstract

The NRC (Nucleotide-binding leucine-rich repeat protein (NLR)-required for cell death) family represents a group of helper NLRs that are required by sensor NLRs to execute cell death during pathogen infection. NRC proteins are classified as CNL, which contain a coiled-coil (CC) domain in their N-terminal region. Previous studies highlighted the importance of the MADA motif in the first alpha helix of the CC domain for NRC-mediated defense responses. However, how other alpha helices in the CC domain contribute to NRC function remains unclear. In this study, we identified a novel hydrophobic feature localized in the CC domain barrel that contributes to NRC-mediated immunity. We screened the conserved hydrophobic residues among NRCs and identified seven required for NRC4-mediated cell death. Structural analysis revealed that four of these residues form a hydrophobic center in the CC domain. We further demonstrated that this hydrophobic core is important for NRC4 subcellular localization, oligomerization, and phospholipid association, but not for NRC4 focal accumulation on the extra-haustorial membrane during *Phytophthora infestans* infection. By comparing sequences of multiple NLRs in the NRC superclade, we found that the residues of the hydrophobic core in sensor NLRs exhibit greater diversity than those in helper NLRs. Cell death assays indicated that the function of the hydrophobic core has degenerated in certain sensor NLRs but remains essential in NRCs and ZAR1. Overall, our study highlights a novel hydrophobic feature in the CC domain of the NRC and its contribution to NLR-mediated immunity.

Keywords: plant immunity, nucleotide-binding leucine-rich repeat protein (NLR), NLR-required for cell death (NRC), resistosome, coiled-coil domain

Significance

Plant intracellular immune receptors known as NRCs (NLR-required for cell death) form resistosome complexes to activate pathogen defense, yet the contributions of coiled-coil (CC) domain features beyond the MADA motif remain unclear. Here, we uncover a novel hydrophobic core in the CC domain of NRC4 that is critical for subcellular localization, oligomerization, and phospholipid association, and thus for effective immune signaling. Intriguingly, while this hydrophobic feature is highly conserved among helper NRCs and singleton NLR ZAR1, the corresponding amino acid residues show greater sequence diversity or has been functionally degenerated in most other sensor NLRs, suggesting a divergence in sequences and in function. Our findings highlight the importance of this previously uncharacterized structural element for NRC-mediated cell death.

54 **Introduction**

55

56 As immobile organisms, plants cannot escape from pathogen attacks. To defend against
57 pathogen colonization, plants have evolved sophisticated immune receptor systems that
58 allow the detection and rapid response to pathogen infection (1–3). Among these receptors,
59 nucleotide-binding leucine-rich repeat proteins (NLRs) serve as intracellular immune
60 sensors, recognizing pathogen effectors and initiating hypersensitive cell death to limit
61 pathogen proliferation (1, 4).

62

63 NLRs consist of three canonical domains: the N-terminal domain, the NB-ARC domain, and
64 the LRR domain (4). Based on the nature of their N-terminal domains, NLRs are classified
65 into three main types: CC-NLRs (CNL), which contain a coiled-coil (CC) domain; TIR-NLRs
66 (TNL), which contain a Toll/interleukin-1 receptor (TIR) domain; and CC_R-NLRs (RNL), which
67 possess a Resistance to Powdery Mildew 8 (RPW8)-like domain (4). These N-terminal
68 domains provide a diverse function for the NLR to trigger immunity. In TNLs, the TIR domain
69 functions as a NADase enzyme, producing phosphoribosyl adenosine
70 monophosphate/diphosphate (pRib-AMP/ADP) or cyclic ADPR (cADPR) isomers that initiate
71 immune signaling (5–9). Mutations in the enzymatic residues essential for NADase activity
72 disrupt immune signaling and impair TNL function (5, 10). Recent studies on CNL and RNL
73 demonstrated that the CC domain plays a crucial role in membrane association and
74 CNL/RNL likely functions as a calcium-permeable channel upon activation to initiate cell
75 death (11–13). Mutations in the positively charged residues involved in membrane
76 association or the negatively charged residues critical for ion channel activity disrupt cell
77 death mediated by some CNL and RNLs (12–15).

78

79 Some NLRs, such as ZAR1, act as functional singletons that recognize effectors and initiate
80 downstream immune responses (11, 16). In some other cases, NLRs have undergone
81 functionalization specialization, evolving into sensor NLRs that detect effectors and helper
82 NLRs that activate the immune response (16–19). The NLR required for cell death (NRC)
83 family represents a group of helper NLRs, forming the NRC network with several
84 phylogenetically related sensor NLRs that are particularly expanded in asterids (17, 20, 21).
85 In solanaceous plants, NRC2, NRC3, and NRC4 are the three major NRCs that function with
86 various sensor NLRs, forming a complex immune network against a broad range of
87 pathogens (17). Some sensor NLRs rely on a single NRC for immunity signaling, while
88 others utilize multiple NRCs, highlighting the genetic redundancy within the NRC network.
89 For example, the sensor NLR *Rpi-blb2*, which detects the RXLR effector AVRblb2 delivered

90 by *Phytophthora infestans*, signals through NRC4, whereas another sensor NLR, Rx, which
91 detects coat protein of potato virus X, signals through NRC2/3/4 in *N. benthamiana* (17).
92
93 Recent cell biology and cryo-EM studies indicated that NRCs switched from cytosolic dimer
94 complexes at the resting state to membrane-associated hexameric resistosome complexes
95 upon activation (22–25). In the resting state, two NbNRC2 protomers dimerize in a specific
96 relative orientation to form a homodimer in the cytosol (25). Notably, the interaction interface
97 of the homodimer varies among different NRCs but is conserved within each NRC group.
98 The unique dimerization interface, which mediates the formation of NRC homodimers rather
99 than heterodimers, likely helps to minimize unwanted cross-activation between NRC helpers
100 (25). Additionally, studies on SlNRC2, an ortholog of NbNRC2, revealed that, in addition to
101 homodimers, SlNRC2 assembles into filamentous structures that likely serve to regulate its
102 activity negatively (24). Furthermore, the binding of inositol phosphate to the WHD domain
103 and LRR domain is critical for the function of SlNRC2 (24).

104 Upon activation by the sensor NLR, the NbNRCs homodimer dissociates and oligomerizes
105 into hexameric resistosome complexes localized on the plasma membrane (15, 22). Notably,
106 NbNRC4 resistosomes function as ion-permeable channels, enabling calcium influx that
107 ultimately induces hypersensitive cell death (22). This role of hexameric NRC resistosomes
108 aligns with findings from the pentameric AtZAR1 and TmSr35 resistosomes, which also form
109 ion channels on the plasma membrane to trigger cell death (11, 22, 26).

110 *P. infestans* use haustoria to penetrate plant cells to deliver effectors and obtain nutrients
111 during infection (27, 28). These haustoria are surrounded by a specialized, newly
112 synthesized plant membrane called the extra haustorial membrane (EHM) (28, 29). To
113 successfully colonize the host, *P. infestans* secret a range of RXLR effectors across the
114 EHM to facilitate the infection (30, 31). Among these, the RXLR effector AVRblb2
115 accumulates at the EHM and targets the secretion of papain-like cysteine protease C14,
116 thereby suppressing immune responses (30). Interestingly, NRC4 also focally accumulates
117 at the EHM during *P. infestans* infection, even in the absence of Rpi-blb2 (32). Upon
118 activation by Rpi-blb2, NRC4 forms puncta on both the EHM and parts of the plasma
119 membrane. Recent research underscores the importance of the interactions between NRC4
120 and phosphatidylinositol phosphates, such as PI4P, which also exist on the EHM (15, 33).
121 However, the extent to which NRC4-lipid interactions influence its localization at the EHM
122 and plasma membrane remains to be determined.

123 As a member of the CNL family, the NRC4 protein contains four alpha helices in its CC
124 domain (22). The first alpha helix in the NRC4 CC domain contains a conserved MADA

motif, which is shared by NRC helper proteins and ZAR1 but not NRC-dependent sensor NLRs (34). Mutations of the hydrophobic residues in the MADA motif disrupted NRC and ZAR1-mediated cell death (34). These findings highlight the importance of maintaining the hydrophobicity within the first alpha helix of the CC domain in regulating NRC function. However, how other alpha helices in the CC domain contribute to NRC4 function remains unknown.

In this study, we identified a novel hydrophobic center formed by the α2–α4 helices of the NRC4 CC domain, which plays a critical role in NRC4-mediated immunity. Mutations in this hydrophobic core impaired NRC4 resistosome formation and NRC4-phospholipids association. Interestingly, these mutations did not affect the subcellular localization of NRC4 in its resting state or its focal accumulation at the EHM during *P. infestans* infection. Further investigation revealed that the corresponding residues in this hydrophobic core are highly conserved in ZAR1 and NRC, but have diverged in certain sensor NLRs. Moreover, while this hydrophobic feature is functionally significant in ZAR1 and NRC, it appears less critical in some sensor NLRs. In summary, we identified a new hydrophobic element at the center of the CC domain that is essential for NRC4 resistosome formation and phospholipid binding, and is conserved across NRC and ZAR1.

Results

Mutations of conserved hydrophobic residues in the CC domain compromise the cell death activity of NRC4

The N-terminal CC domain in CNL comprises four alpha helices (α1~α4) that are crucial for resistosome function (11, 22). In NRC4 as well as most other NRCs, the α1 helix is known to contain a MADA motif essential for mediating cell death (34). However, how α2-4 helices in the CC domain contribute to the NRC function is not clear. To dissect the function of these alpha helices in NRC4-mediated cell death, we perform the full-length protein sequence alignment of NRC4 with NRC2, NRC3, and AtZAR1. We found 19 conserved hydrophobic residues across the three α-helices of NRCs and AtZAR1 (Fig. S1). To further identify which residues are essential to the function of NRC4, we mutated those hydrophobic residues (L/A/I/V/F) into the hydrophilic residue glutamic acid (E). We then tested their cell death activities by co-expression with Rpi-blb2 and AVRblb2 in the *nrc2/3/4*_KO *N. benthamiana* and quantified the cell death by using auto-fluorescence-based imaging (Fig. 1A). Out of the 19 NRC4 variants, we found that single mutations at L34, F44, A72, I114, V118, L121, and L128 significantly impaired NRC4-mediated cell death (Fig. 1B-D). The protein accumulation

levels of these NRC4 mutants with compromised cell death show no significant difference compared to the wild-type (Fig. S2A, B), indicating that the reduced NRC4-mediated cell death is not due to changes in protein accumulation. In total, we identified mutations of 2 residues in α2, 1 residue in α3, and 4 residues in α4 of CC domains that compromised the NRC4-mediated cell death.

To test whether these 7 mutations also compromise the cell death induced by an autoactive NRC4 mutation, we introduced these mutations individually into the NRC4^{D478V} which contains a mutated MHD motif leading to sensor-independent cell death. Most of these mutations also completely impair NRC4^{D478V}-mediated cell death, except for L121E. While the NRC4^{L121E} mutation failed to induce cell death with Rpi-blb2/AVRblb2, NRC4$^{L121E/D478V}$ induced strong cell death (Fig. 1E). This suggests that residue L121 may play a role in the cooperation between NRC4 and its sensor NLRs. As we decided to focus on the intrinsic feature of the NRC4 CC domain, we excluded L121 from our further analyses. In summary, we identified six key hydrophobic residues in the α2 to α4 of the CC domain that contribute to NRC4-mediated cell death.

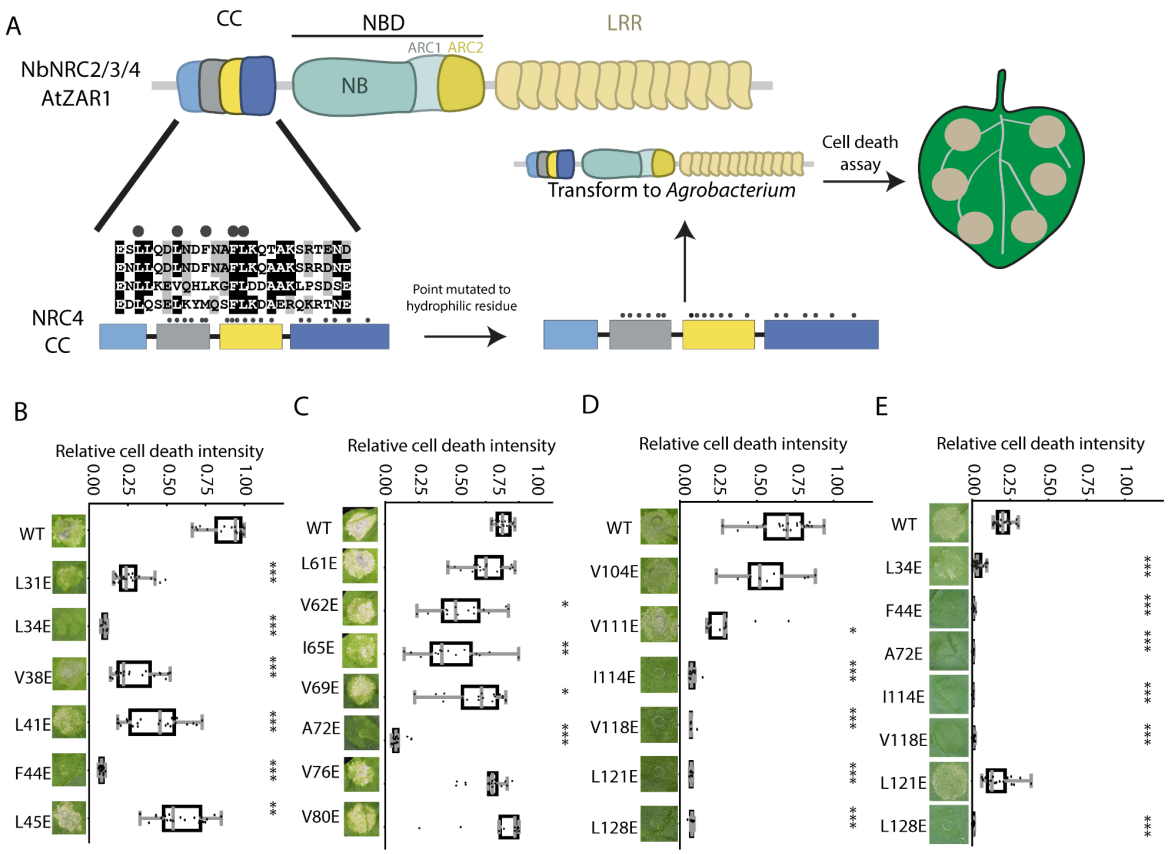

Figure 1. Mutation of conserved hydrophobic residues in the CC domain affects the cell death activity of NRC4.

(A) Experimental design for screening key hydrophobic residues in the NRC4 CC domain. Conserved hydrophobic residues shared by NRC2/3/4 and AtZAR1 were selected and mutated to glutamic acid. The generated NRC4 variants were then tested in cell death assays. (B)(C)(D) Cell death assays of NRC4 hydrophobic core variants, co-expressed with Rpi-blb2 and AVRblb2 in *nrc2/3/4*_KO *N. benthamiana*. Cell death intensity and phenotypes were recorded at 6 days post-infiltration (dpi). (E) Cell death assays of autoactive NRC4 variants with candidate hydrophobic residue mutations identified in panels (B)–(D). The central line in each box plot represents the median cell death intensity, with box edges indicating the 25th and 75th percentiles. The whiskers extend to the most extreme data points no more than 1.5x of the interquartile. Statistical differences between wild-type and variant samples were analyzed using paired Wilcoxon signed rank test (*=p<0.01, **=p<0.005, ***=p<0.00001).

The identified residues form a hydrophobic center in the CC domain

Using NRC2 (PDB: 8RFH) as a reference, we employed Alphafold 3 (AF3) to model the dimer structure of NRC4, including the CC domain that was not captured in the original NRC2 cryo-EM data (Fig. 2, S3, and S4). We discovered that four of these residues (L34/A72/I114/V118) are located in proximity to each other, likely forming a hydrophobic center in the CC domain (Fig. 2A and S3A, B). In contrast, two other residues, F44 of α2 and L128 of α4, are positioned near each other but distant from the hydrophobic core (Fig. 2A). Additionally, we found that the pairwise distances of these four residues in the hydrophobic center (L34, A72, I114, and V118) are predicted to be less than 6Å, indicating potential interactions among them (Fig. 2B). Furthermore, the hydrophobic center of the CC domain is predicted to be concealed by the α1 helix in the resting state (Fig. 2C). Interestingly, the predicted distance from L34 and A72 to L13 of α1, which is a critical residue in the MADA motif, is within 6Å, suggesting the potential interaction between the hydrophobic center and MADA motif (Fig. 2C). These observations imply that this hydrophobic core in the CC domain may play a role in NRC4 function by interacting with the MADA motif.

At the activated state, NRC4 forms a hexameric resistosome (22). This hydrophobic core is embedded in the CC domain inside the activated resistosome complexes (Fig. 2D). The EDVID motif of α3 interacts with the R-cluster in the LRR domain, which is crucial for the NRC4 function (22). We observed that A72, one of the residues in the hydrophobic center, is located near the EDVID motif but does not directly participate in the interaction between the EDVID motif and the R-cluster (Fig. S3C). Furthermore, F44 and L128, the other two residues not part of the hydrophobic center, localize near the putative ion conducting core (Fig. 2D). Our results suggest that this hydrophobic core in the NRC4 CC domain may directly or indirectly influence the intramolecular interactions among different motifs.

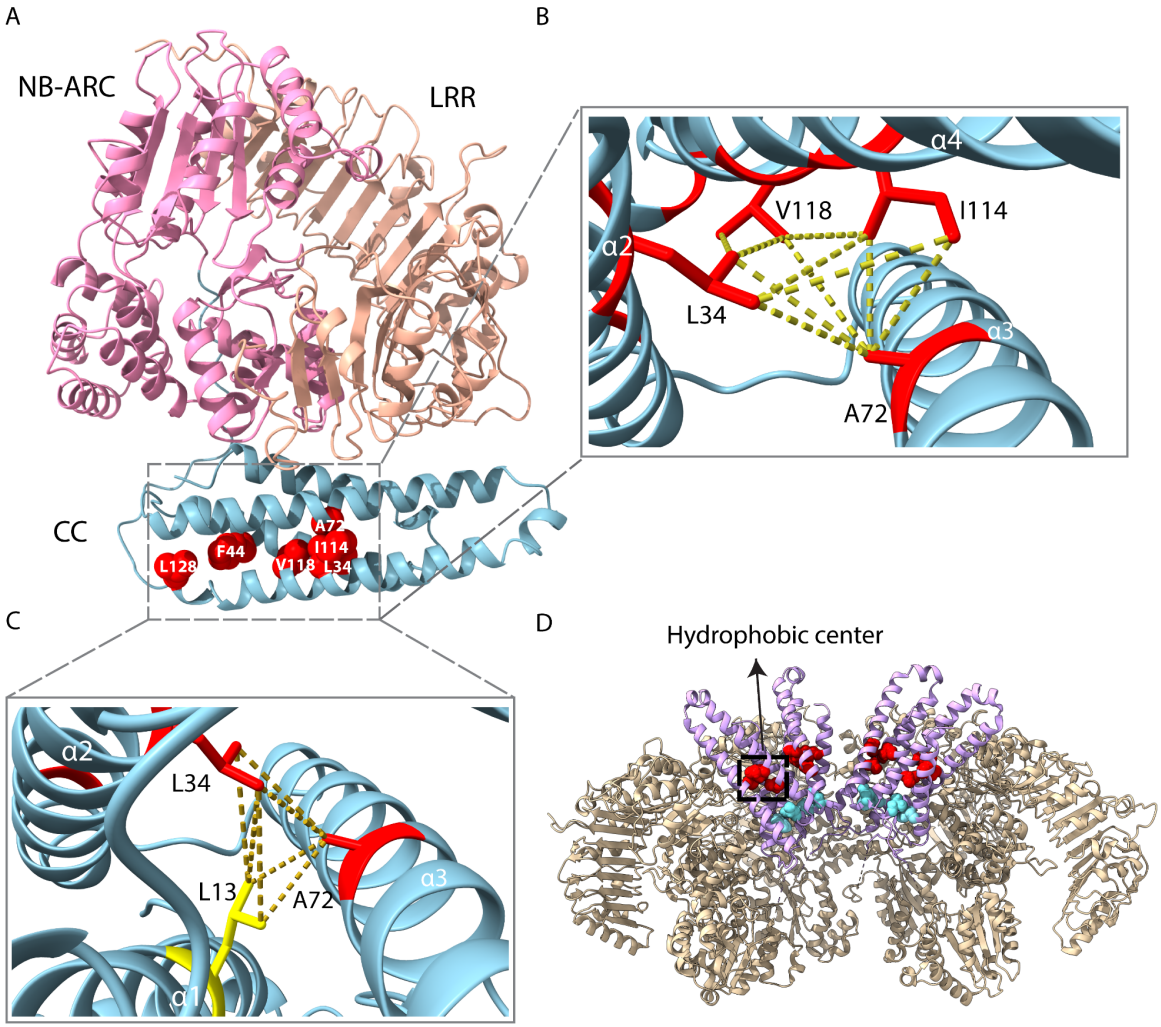

Figure 2. Four of the identified residues form a hydrophobic core at the center of the NRC4 CC domain. (A) The predicted NbNRC4 structure derived from the NbNRC2 cryo-EM structure (PDB: 8RFH). The coiled-coil (CC) domain is shown in cyan, the NB-ARC domain in light pink, and the LRR domain in beige. Hydrophobic residues of interest are highlighted in red. (B) and (C) The positions of the hydrophobic center residues (red) and L13 (yellow) on the MADA motif in the α1 helix. Dashed lines represent putative interactions where side-chain distances are less than 6 Å. (D) The location of the hydrophobic core in the NRC4 resistosome (PDB: 9CC8). For simplicity, only four of the six NRC4 protomers are displayed. The CC domains are shown in purple, with the remaining regions in gold. Hydrophobic core residues are highlighted in red, and two additional residues outside the core are indicated in cyan.

Mutation of the hydrophobic center affects NRC4 punctate formation

NRC4 localizes in the cytoplasm at the resting state, and forms membrane-associated puncta upon activation (32). To test whether the hydrophobic core contributes to the NRC4 subcellular localization in both resting and activated states, we tagged the NRC4 variants with the C-terminal GFP tag and performed cell biology experiments. Since wild-type NRC4 induces fast and robust cell death, limiting the application of wild-type NRC4 in cell biology studies, we employed the NRC4$^{L9A/V10A/L14A}$ variant (NRC4^{AAA}) for cell biology analysis (34).

234 The NRC4^{AAA} variant, which carries mutations in the MADA motif, displays weaker and
235 delayed cell death responses, allowing for cell biology analysis (Fig. S5). We, therefore,
236 used the NRC4^{AAA} variant as the background for subsequent NRC4 functional analyses.

237 We co-expressed NRC4 variants with Rpi-blb2 to investigate their subcellular localization in
238 the resting state. We observed that the NRC4^{AAA} variant predominantly localized in the
239 cytosol at the resting state, consistent with the previously reported localization of wild-type
240 NRC4 (15, 32) (Fig. S6). Similarly, all four hydrophobic core mutants (L34E, A72E, I114E,
241 and V118E) also predominantly localized in the cytosol at the resting state, indicating that
242 mutations in the hydrophobic core do not lead to mislocalization.

243 To test whether the hydrophobic center affects NRC4 localization upon activation, we co-
244 expressed the NRC4 mutants with Rpi-blb2 and its recognized effector AVRblb2. Upon
245 activation, the NRC4^{AAA} variant exhibited a dramatic change in subcellular localization,
246 forming membrane-associated punctate (Fig. 3A), consistent with the previous finding on the
247 NRC4^{L9E} variant (32). Interestingly, hydrophobic core mutants remained in the cytosol when
248 co-expressed with Rpi-blb2 and AVRblb2, suggesting that these mutations impair the ability
249 of NRC4 to undergo activation-induced relocalization. However, the A72E mutant could still
250 form a few membrane-associated punctate structures upon Rpi-blb2 activation (Fig. 3A). We
251 quantified cells with NRC4^{AAA} and NRC4^{A72E} punctate at 2 and 3 days post-inoculation (dpi)
252 and found that NRC4^{A72E} exhibited delayed punctate formation (Fig. S7A). These findings
253 suggest that NRC4^{A72E} has reduced efficiency and requires more time to oligomerize than
254 NRC4^{AAA}. Our results indicate that the hydrophobic core contributes to NRC4 punctate dot
255 formation upon activation of Rpi-blb2.

256

257 **Mutation of the hydrophobic center compromises NRC4 oligomerization**

258 NRC4 oligomerizes into a hexameric resistosome upon activation (22, 35). To determine
259 whether mutations in the hydrophobic core affect NRC4 oligomerization, we conducted the
260 Blue Native- Polyacrylamide gel electrophoresis (BN-PAGE) analysis using C-terminal Myc-
261 tagged NRC4 variants. NRC4 and Rpi-blb2 were co-expressed with or without AVRblb2, and
262 total proteins were collected for BN-PAGE analysis at 2 days after agroinfiltration. Consistent
263 with the previous report using NRC4^{L9E}, NRC4^{AAA} migrates as a ~240 kDa complex at the
264 resting state, and a ~900 kDa complex at the activated state (35). We found that the
265 hydrophobic core mutations are disrupted in oligomerization, keeping NRC4 in a dimeric
266 state in the presence of both AVRblb2 and Rpi-blb2 (Fig. 3B). Consistent with the cell
267 biology assays, the NRC4^{A72E} mutant retains the ability to oligomerize at 3 days after
268 agroinfiltration, forming a ~900 kDa band similar to the NRC4^{AAA} upon activation (Fig. S7B).

269 Overall, these results indicate that the hydrophobic core plays a critical role in NRC4
270 oligomerization.

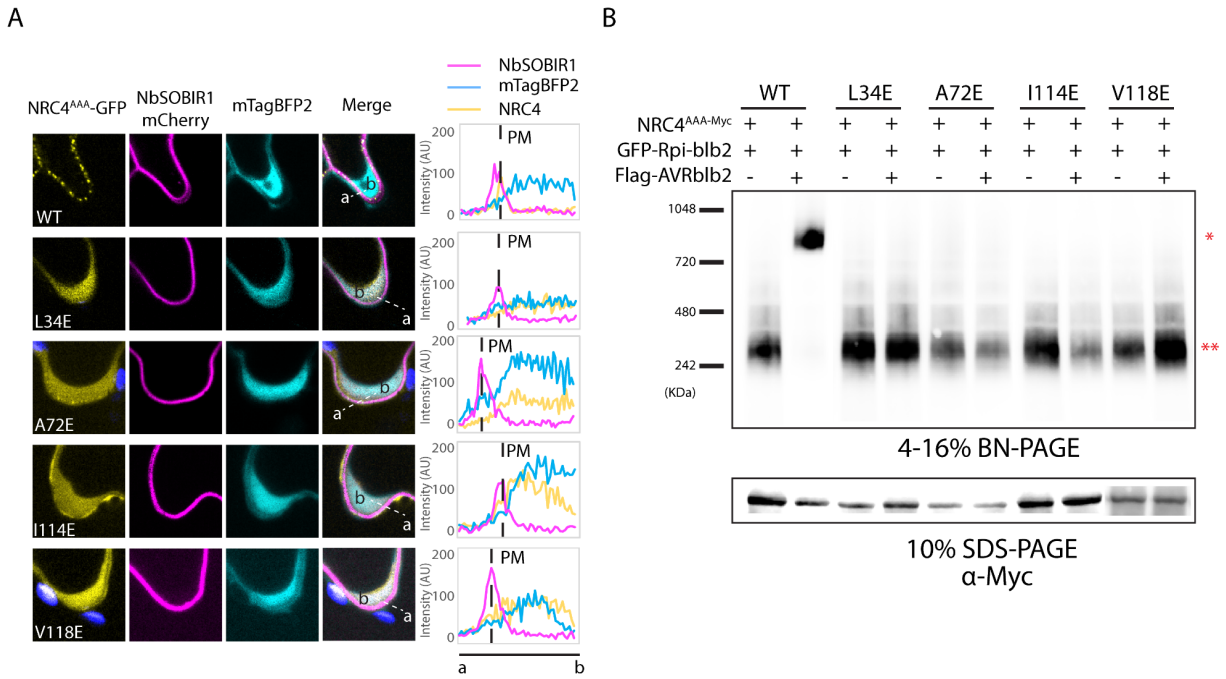

271

272 **Figure 3. Mutations in the hydrophobic center disrupted NRC4 punctate formation and oligomerization.**
273 (A) Confocal images showing the subcellular localization of transiently expressed GFP-tagged NRC4^{AAA} and
274 hydrophobic center mutants with SOBIR1-mCherry (plasma membrane marker) and mTagBFP2 (cytosol marker)
275 in *nrc2/3/4*_KO *N. benthamiana* leaves co-expressing Rpi-blb2 and AVRblb2. Images were captured at 2 days
276 post-infiltration (dpi). The lines in the overlay panel indicate the region selected for measuring the fluorescence
277 intensity of each channel. The blue signal corresponds to the chloroplast. The intensity was measured from
278 position "a" to "b," and values are reported in arbitrary units (AU). (B) Upper panel: BN-PAGE analysis showing
279 the formation of the NRC4^{AAA} and hydrophobic center mutant resistosomes. NRC4 variants and Rpi-blb2 were
280 transiently expressed in *nrc2/3/4*_KO *N. benthamiana* leaves, with and without AVRblb2. Lower panel: Western
281 blot analysis of SDS-PAGE to confirm NRC4 protein expression levels. Total protein samples were collected at 2
282 dpi for both BN-PAGE and SDS-PAGE. Approximate molecular weights (kDa) are indicated on the left. A single
283 asterisk (*) indicates the NRC4 resistosome, while a double asterisk (**) denotes the NRC4 dimer in the BN-
284 PAGE data.
285

286 **The hydrophobic center contributes to the NRC4-phospholipid association**

287 A previous study demonstrated that five residues (K84, K87, K89, K91, and R94) within the
288 disordered region of the NRC4 CC domain play a role in its association with phospholipids
289 (15). To explore whether residues in the hydrophobic center in alpha helices also contribute
290 to NRC4-phospholipid interactions, we performed a phospholipid-binding assay using PIP
291 strips. We conducted the wheat-based in vitro translation to express the CC domain of
292 NRC4^{AAA} and corresponding hydrophobic center mutants (Fig. 4A). After confirming
293 accumulations, we incubated proteins with PIP strips to determine the association between

294 NRC4 CC domain and phospholipids. The fluorescent protein mCherry was used as a
295 negative control for the background binding of this experiment.
296
297 We found that the NRC4^{AAA} CC domain is associated with the PI4P and PI(4,5)P_2, which is
298 consistent with the previous report using the wild-type NRC4 CC domain (Fig. 4B) (15).
299 Additionally, we observed the binding of NRC4^{AAA} to other phospholipids, including PI-
300 monophosphate-PI3P, PI5P, and PI biphosphate-PI(3,4)P_2, PI(3,5)P_2, phosphatidic acid
301 (PA) and phosphatidylserine (PS) (Fig. 4B). However, we observed that the negative control
302 mCherry also binds to PA and PS, suggesting that the signals detected with PA and PS are
303 the results of background binding in our assay.
304
305 In contrast, all variants harboring mutations in the hydrophobic core showed a much-reduced
306 ability to bind either the mono- or biphosphate forms of PI (Fig. 4B). All hydrophobic core
307 mutants exhibited detectable protein accumulation levels, although variants A72E and I118E
308 showed reduced accumulation (Fig. 4B). We next examined the lipid-binding ability of the
309 two variants carrying mutations outside the hydrophobic center (F44E and L128E), both of
310 which impaired NRC4-mediated cell death. These mutations did not affect the interaction of
311 the NRC4 CC domain with phospholipids (Fig. S8). Overall, our findings indicate that
312 residues within the hydrophobic core are indispensable for NRC4-phospholipid association,
313 whereas residues outside the core, such as F44 and L128, do not contribute to this
314 association.

315 Next, we conducted a cell fractionation assay to assess the degree mutations in the
316 hydrophobic core influence membrane association of NRC4 under resting conditions and in
317 the presence of Rpi-blb2 and AVRblb2. Under resting conditions, NRC4^{AAA} was detected in
318 both the soluble and membrane fractions (Fig. 4C). Upon activation of Rpi-blb2, NRC4^{AAA}
319 became enriched in the membrane fraction, consistent with previous findings (32) (Fig. 4D).
320 Similarly, hydrophobic core mutants of NRC4 were present in both fractions under resting
321 conditions (Fig. 4C). In contrast to NRC4^{AAA}, upon co-expression of Rpi-blb2 and AVRblb2,
322 these hydrophobic core mutants failed to exhibit enhanced membrane association (Fig. 4D).
323 Instead, their protein levels in the soluble and membrane fractions remained comparable to
324 those observed under resting conditions (Fig. 4C,D). These results suggest that, although
325 NRC4 hydrophobic core mutants lose their ability to bind phospholipids, they may still
326 associate with membranes. Furthermore, these impaired NRC4-membrane association
327 dynamics are consistent with cell biology observations showing that the hydrophobic core
328 mutants fail to relocalize to the plasma membrane in the presence of Rpi-blb2 and AVRblb2.

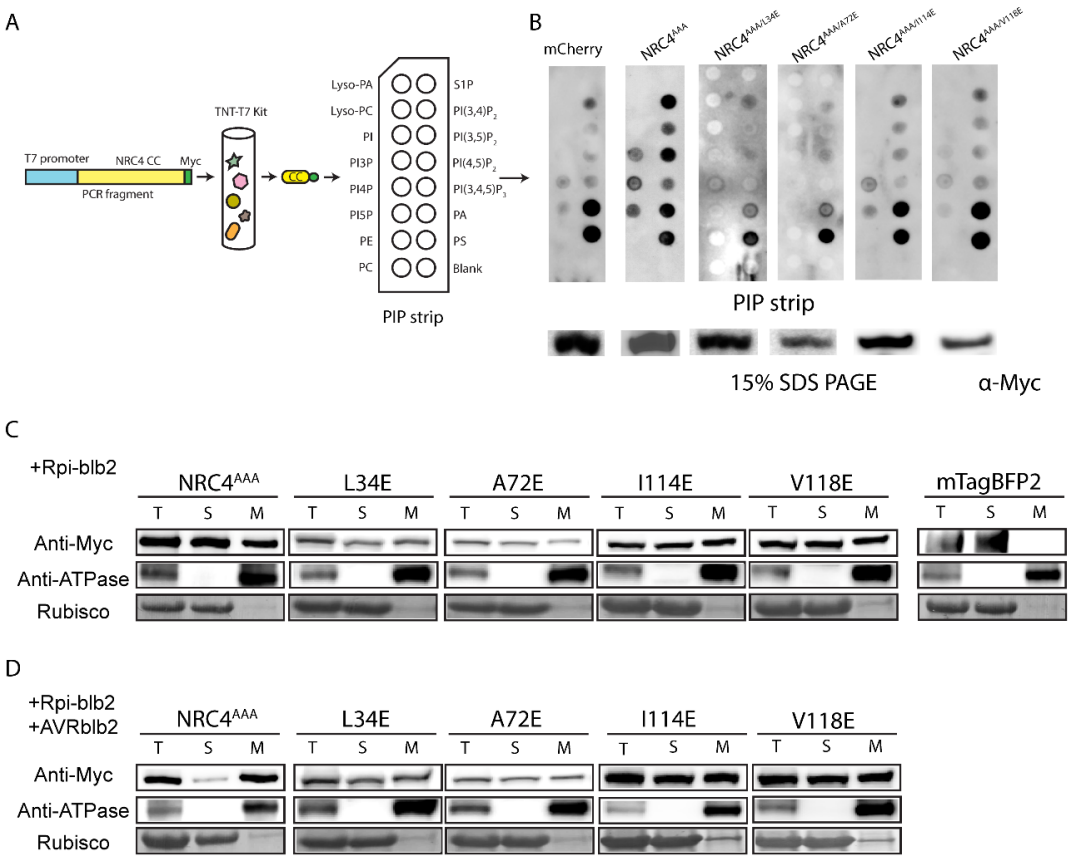

Figure 4. The mutation of the hydrophobic center compromised the NRC4 phospholipid association and spatial dynamics.

(A) Experimental setup for investigating the association between the NRC4 CC domain and phospholipids. A gene fragment encoding the NRC4 CC domain with a C-terminal 4×Myc tag was amplified by PCR and in vitro translated using the TNT Coupled Wheat Germ Extract System. The resulting protein extract was directly incubated with a PIP strip for the lipid association assay, and the NRC4 CC domain was detected using an anti-Myc antibody. (B) Phospholipid-binding assay for various NRC4 mutants. Myc-tagged mCherry served as a negative control. Expression levels of the in vitro-translated NRC4 CC domain variants were confirmed by western blot (shown below the assay data). (C) and (D) Membrane enrichment assay assessing the localization of NRC4 and NRC4 hydrophobic core mutants co-expressed with Rpi-blb2, with or without AVRblb2. Leaf samples were collected at 2 days post-infiltration (dpi), and total protein extracts were separated into soluble (S) and membrane (M) fractions. NRC4 proteins were detected using an anti-Myc antibody. An ATPase enzyme served as the membrane marker, and Rubisco is enriched in the soluble protein fraction. T represents the total extract. Rubisco was visualized by Coomassie blue staining.

Disruption of the hydrophobic center does not affect haustoria accumulation of NRC4

NRC4 accumulates around the extra haustorial membrane (EHM) of *P. infestans* during infection, likely facilitating effector detection (32). To investigate whether residues in the hydrophobic core are important for NRC4 focal accumulation on EHM, we expressed NRC4^{AAA} or its hydrophobic core mutants in *nrc2/3/4_KO N. benthamiana* leaves. At one day post-agroinfiltration (dpi), we inoculated the detached leaves with *P. infestans* zoospores and examined the localization of NRC4 variants 2 days after pathogen inoculation.

352 Consistent with previous reports on NRC4^{WT}, NRC4^{AAA}-GFP focally accumulated on the
353 EHM (Fig. 4) (32). Similarly, all the tested NRC4 mutants displayed sharp signals around the
354 EHM, but not in the cytosol or on the plasma membrane, in the haustoriated cells (Fig. 4).
355 We further utilized the NRC4^{WT}-RFP as the EHM marker to validate the accumulation of our
356 NRC4 mutants. We observed that the NRC4 hydrophobic core mutants co-localized with the
357 NRC4^{WT}-RFP, indicating our hydrophobic core mutants maintain their capacity for EHM focal
358 accumulation (Fig. S9). These findings suggest that the hydrophobic center in the NRC4 CC
359 domain does not contribute to its focal accumulation at the EHM.

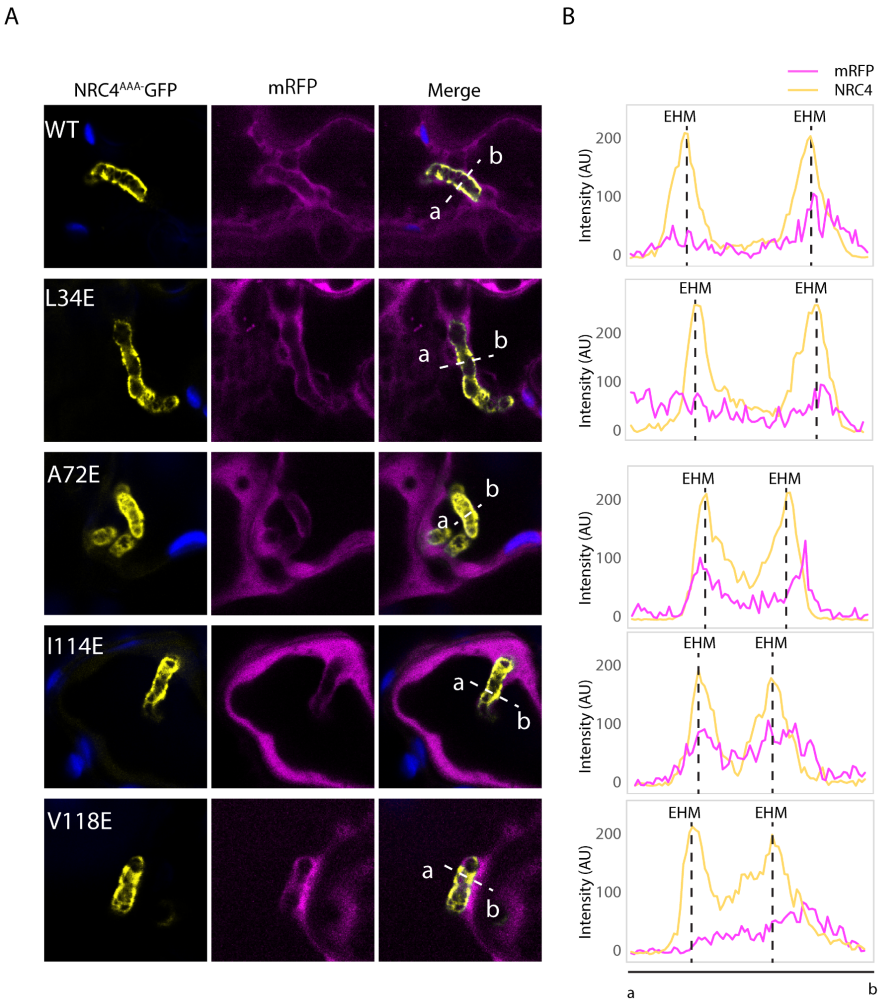

360
361 **Figure 5. Mutations in the hydrophobic center did not affect NRC4 focal accumulation on EHM.**
362 Confocal images showing the accumulation of NRC4^{AAA} and hydrophobic center variants on the EHM. The NRC4
363 variants, tagged with C-terminal GFP, were transiently expressed with the mRFP (cytosol marker) in the
364 *nrc2/3/4_KO N. benthamiana* leaves. At 1 dpi, *P. infestans* zoospores were inoculated onto detached leaves and
365 incubated for two more days. Images were taken at 3 dpi. The lines marked on the overlay panel indicated the
366 selected region for measuring the intensity of each channel. The blue signal represents the chloroplast.
367 Fluorescence intensity was measured from position “a” to “b” in each group, and the values are presented as
368 arbitrary units (AU).
369

370 **The hydrophobic core in the CC domain is essential for singleton NLR ZAR1 and**
371 **helper NLR NRCs**
372 Our findings revealed a novel characteristic of the CC domain, prompting us to investigate its
373 conservation in NLRs within the NRC superclade and related singleton NLRs like R2 and
374 ZAR1. To this end, we selected 22 species representing different genera within the
375 solanaceous family from the recently published solanaceous NLRome dataset (36). We
376 extracted 2,581 NLR sequences and grouped them into phylogenetic clades based on their
377 NB-ARC domain (Fig. 6A, Fig. S10, File S1). Many of the sensor NLRs in the NRC
378 superclade feature N-terminal extensions, which are expected to influence the canonical
379 properties of the CC domain. Therefore, these sensor NLR clades were excluded from
380 further analysis. We then identified the corresponding hydrophobic core residues in each
381 CNL clade and analyzed their polymorphisms.

382 The hydrophobic core residues in the G8 (NRC) clade were highly conserved, with most
383 sequences containing LAIV, similar to *N. benthamiana* NRC4 (Fig. 6B). Entropy analysis
384 showed that these residues had low entropy values, with the highest being 0.75 at position
385 118 (Fig. 6B). Similarly, the hydrophobic core residues of the G5 (R2) and ZAR1 clades
386 were also highly conserved, predominantly featuring LALI or LAII, respectively. Entropy
387 analysis revealed that the G5 clade had entropy values below 0.75, with the ZAR1 clade
388 showing no variation (entropy value 0) at these positions (Fig. 6B, Dataset S3, File S2).

389 For NRC-dependent sensor NLR clades, such as G12 (Rx), G2 (Bs2), G14 (Rpi-amr1), and
390 G9 (Rpi-amr3), most of the corresponding residues maintained their hydrophobicity, though
391 some positions had lost this property (Fig. 6B). For instance, in the G2 (Bs2) clade, the
392 residue corresponding to V118 was replaced by serine in a subset of the 116 sequences
393 analyzed. In the G12 and G9 clades, residues corresponding to A72 and I114 were
394 substituted with threonine in some sequences. At least one position in these sensor NLR
395 clades exhibited an entropy value greater than 0.75, the maximum entropy observed for the
396 hydrophobic core residues in the NRC group (Fig. 6B, Dataset S3, File S2). These findings
397 suggest that sensor NLR clades have undergone more diversification in their hydrophobic
398 core residues compared to helper NLRs like NRCs and singleton NLRs such as ZAR1.

399 To test the hypothesis that the functional contribution of the hydrophobic core is essential in
400 NRC and ZAR1 clades but has degenerated in NRC-dependent sensor NLRs, we introduced
401 point mutations on the hydrophobic core in the representative NLRs of each clade. We co-
402 expressed the NbNRC2/3 hydrophobic core mutants with Pto and AvrPto, which leads to Prf-

403 and NRC2/3-dependent cell death, in the *nrc2/3/4_KO* plants. Our results showed that all the
404 mutants on the hydrophobic core of NbNRC2/3 compromised the NRC-mediated cell death,
405 suggesting the importance of the hydrophobic core in the activities of both NRC2 and NRC3
406 (Fig. 6D, Fig. S11 A, B).

407 Then, we introduced the hydrophobic core mutations into NbZAR1^{D481V} and R2 to evaluate
408 their importance. Our cell death assays demonstrated that all hydrophobic core mutations in
409 NbZAR1 significantly compromised its ability to mediate hypersensitive cell death,
410 underscoring the critical role of the hydrophobic core in NbZAR1 function (Fig. 6D, Fig. S11
411 C, D). Interestingly, mutations at L34 and L113 of R2 did not affect R2-mediated cell death,
412 whereas V72E and I117E mutations impaired R2 function. This implies that the roles of
413 certain hydrophobic core residues in R2 may have been degenerated.

414 We further explored the importance of the hydrophobic core in NRC-dependent sensor NLRs
415 by introducing core mutations into Rx, Bs2, Rpi-amr1, and Rpi-amr3 (Fig. 6D, Fig. S12).
416 These wild-type and core-mutated sensor NLRs were co-expressed with their corresponding
417 effectors in wild-type *N. benthamiana* leaves. In the cell death assays, hydrophobic core
418 mutations did not affect Rx- or Rpi-amr3-mediated cell death, and most mutations had minor
419 impacts on Rpi-amr1-mediated cell death besides, L37E (Fig. 6D). Interestingly, in Bs2, most
420 hydrophobic core mutations compromised cell death, except for the S119E mutant, which
421 retained functionality. These results indicate that the significance of this hydrophobic feature
422 has partially diminished in certain NRC-dependent sensor NLRs (e.g., Bs2 and Rpi-amr1)
423 and has become nonessential in other NRC-dependent sensor NLRs (e.g., Rx and Rpi-
424 amr3).

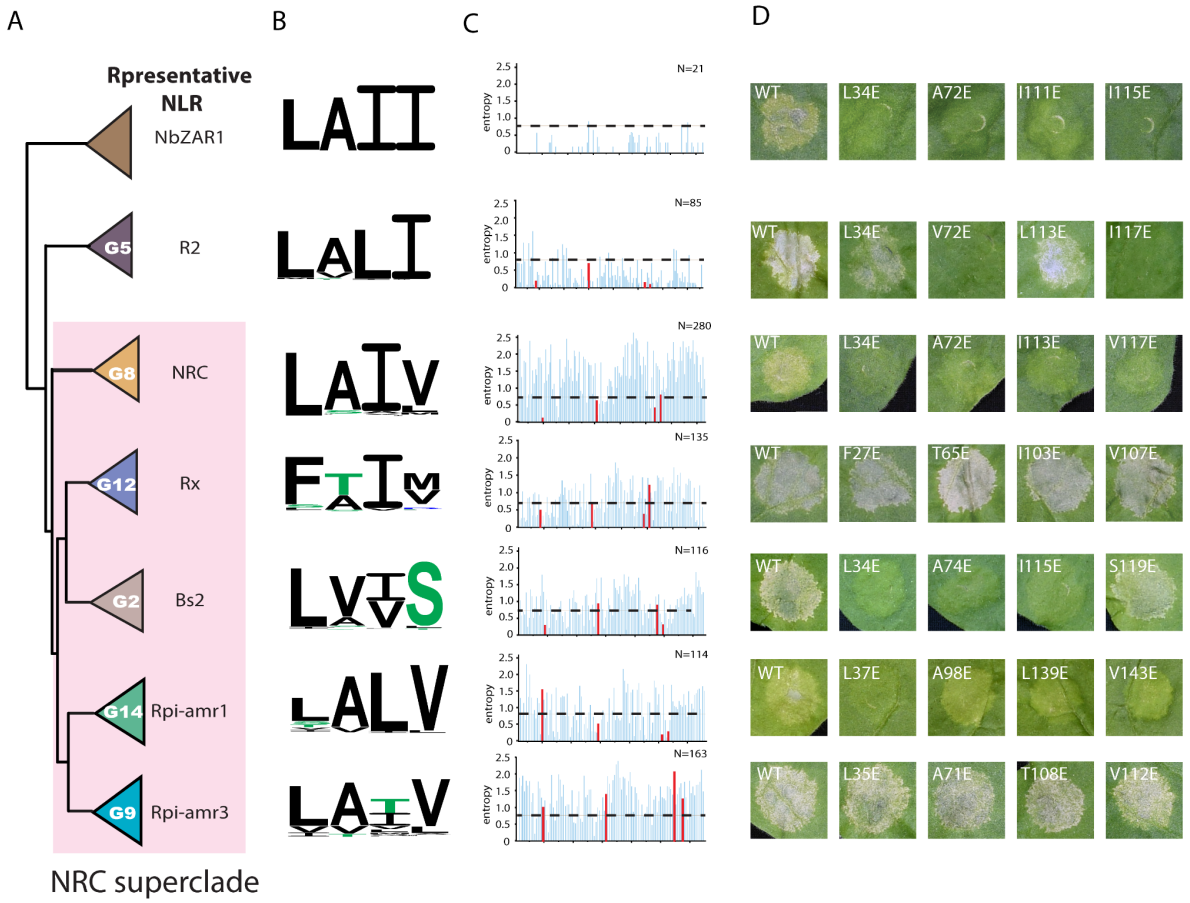

Figure 6. The hydrophobic center in the CC domain is essential for NRC helper NLR and ZAR1. (A) The phylogenetic tree of the NRC superclade and related singleton NLRs, ZAR1 and R2. A representative NLR is indicated for each group. The NRC superclade is highlighted in pink. Sensor NLR clades possessing N-terminal extensions were excluded from this analysis. (B) The amino acid composition of the hydrophobic center in each group is shown in the logo. Hydrophobic residues (AVLIPWFM) appear in black, hydrophilic residues (DE) in red, positively charged residues (KRH) in blue, and polar residues (STN) in green. From left to right, the corresponding residues in NRC4 are L34, A72, I114, and V118. (C) Entropy values for the CC domain of the singleton NLR ZAR1, R2, and the NRC superclade, with the respective hydrophobic core residues in each clade highlighted in red. The number of NLR sequences in each clade is indicated in the top-right corner of the entropy panel. (D) The cell death outcomes following hydrophobic core mutations in representative NLRs from each clade, recorded at 3 dpi. Quantitative data for these cell death assays can be found in Figures S11–S12.

Discussion

While recent cryo-EM studies unveiled the detailed structure of NRC complexes in both resting and activated states, the precise structural features of the CC domain were not fully resolved, likely due to the high flexibility of the region connecting the CC and NB-ARC domains(22, 23, 25). Expanding on the previously established knowledge of the MADA motif in the α1 helices, our study identified several conserved hydrophobic residues across NRCs

445 within the α2 to α4 helices (Fig. S1). We further demonstrated that several of these
446 hydrophobic residues, situated at the core of the CC domain, form a hydrophobic core
447 essential for NRC4 function (Fig. 1 and 2).

448 Several CNL-type singleton and helper NLRs undergo dynamic subcellular transitions from
449 the cytosol to the plasma membrane, where they form pentameric or hexameric resistosome
450 complexes upon activation (11, 12, 22, 32). We found that mutations in the hydrophobic core
451 do not affect the subcellular dynamics of NRC4 in its resting state (Fig. S6). However, upon
452 activation of the sensor NLR Rpi-blb2, these mutations hinder NRC4's ability to oligomerize
453 and localize at the plasma membrane (Fig. 3A). Additionally, BN-PAGE analysis showed that
454 the hydrophobic core mutants remain as dimers when co-expressed with Rpi-blb2 and
455 AVRblb2 (Fig. 3B). One possible explanation could be that the hydrophobic core mutant
456 NRC4 is unable to receive the activation signal from the sensor NLR, resulting in its
457 remaining as an inactive homodimer in the cytosol. Alternatively, the hydrophobic core
458 mutant NRC4 can receive the signal, but the mutation altered the CC domain structure,
459 preventing the disruption of the homodimer and the formation of resistosome complexes.

460 While the MADA motif is an essential feature in the α1 helix of NRC4, the detailed
461 mechanism of how the hydrophobic residues on the MADA motif contribute to NRC4 function
462 is still unclear (34). Using AF3 predictions, we showed that the L13 residue, which is critical
463 for the cell death activity of NRC4, within the MADA motif, potentially interacts with two
464 hydrophobic core residues in the α2 and α3 helices (Fig. 2C). The ZAR1 resistosome study
465 proposed a "flipping out" process of the α1 helix in the CC domain during activation of ZAR1,
466 which is a crucial event for ZAR1-mediated cell death (11). Prior structural analysis of the
467 NRC failed to identify the α1 helix of the CC domain in the activated resistosome, implying
468 that the α1 helix might also undergo a "flipping out" process (22, 23). Given the similarity
469 between ZAR1 and NRC resistosomes, we speculate that mutations in this region could
470 disrupt the hydrophobic interactions between the MADA motif and the α2-α3 helices,
471 impairing the "flipping-out" process of the α1 helix during activation and ultimately
472 compromising ZAR1 and NRC function.

473 A recent cryo-EM study showed that a triple mutation within the EDVID motif of the α3 helix
474 disrupts NRC4-mediated cell death, while single mutations in this region do not affect NRC4
475 functionality (22). In contrast, we observed that a single mutation at A72, located adjacent to
476 the conserved EDVID motif in the hydrophobic core, is sufficient to impair NRC4-mediated
477 cell death (Fig. 1C). Interestingly, NRC4 with the A72 mutation can still oligomerize and
478 localize to the plasma membrane at 3 dpi. However, this A72E mutant resistosome is non-
479 functional and unable to trigger cell death. Our findings suggest that A72 likely plays a role in

480 modulating interactions between the EDVID motif and the R-cluster, thus regulating NRC4-
481 mediated cell death (Fig. 1C, Fig. S3C).

482 The interaction between phospholipids and helper NLRs is crucial for NLR-mediated cell
483 death (14, 15). NRC4 has previously been shown to associate with PI4P and PI(4,5)P2, two
484 key phospholipids located on the plasma membrane (15). A positively charged cluster in the
485 α4 helix of NRC4, conserved among other helper NLRs such as ADR1 and NRG1, has been
486 identified as playing a vital role in NRC4-phospholipid interaction (15). In our study, single
487 mutations in the hydrophobic core of NRC4 were found to disrupt its association with
488 phospholipids. Since the hydrophobic core is embedded within the resistosome, it is unlikely
489 to interact with lipids in the activated state directly. A plausible explanation is that these
490 mutations alter the structure of the NRC4 CC domain, disrupting the proper conformation of
491 the positively charged loop and thereby impairing the interaction between NRC4 and
492 phospholipids. Notably, most hydrophobic core mutants of NRC4 lose both their capacity to
493 associate with phospholipids and their ability to oligomerize. Our results supported the
494 hypothesis that the interaction of NRC4 with phospholipids is crucial for resistosome
495 formation. When the CC domain structure is disrupted, NRC4-phospholipid binding is
496 compromised, causing NRC4 to remain as a cytosolic homodimer rather than oligomerizing
497 into functional resistosome complexes.

498 The focal accumulation of NRC4 on the EHM is a distinctive feature observed during *P.*
499 *infestans* infection (32). Interestingly, NRC4 hydrophobic core mutants can still focally
500 accumulate on the EHM during *P. infestans* infection, indicating that these mutations do not
501 affect all the intrinsic features of NRC4. Previous studies on phospholipid composition at the
502 EHM identified PI4P and PI(4,5)P_2 as the primary phospholipids enriched at the EHM (33).
503 However, our lipid-binding assay reveals that hydrophobic core mutations of NRC4 abolish
504 the ability to associate with both PI4P and PI(4,5)P_2. One possible explanation is that the
505 focal accumulation of NRC4 on the EHM may not depend on a direct association of the
506 NRC4 CC domain with lipids. Instead, other regions of the NRC4 canonical domain or
507 interactions with host or pathogen proteins are likely involved in this process. NRC4 may
508 require these additional domains or partnering proteins to facilitate NRC4 focal accumulation
509 on the EHM.

510 Previous studies suggest that NRC helper NLRs and NRC-dependent sensor NLRs arose
511 through sub-functionalization from an ancestral singleton NLR (16). This process likely
512 involved divergence of sequence features, resulting in altered protein functionality. One
513 notable example is the MADA motif, which is conserved among NRC, ZAR1, and some
514 sensor NLRs, but not in NRC-dependent sensor NLRs (34). Similarly, while the hydrophobic

515 core described here is conserved in NRC and ZAR1, it is relatively less conserved—whether
516 in sequence or functionality—among other sensor NLRs (Fig. 6C). We propose that this
517 hydrophobic core emerged in the common ancestral NLR of ZAR1 and NRCs, but
518 subsequently degenerated partially or entirely in NRC-dependent sensor NLRs.

519 Although the hydrophobic sequence feature is present in R2, only two hydrophobic core
520 mutants demonstrated reduced cell death (Fig. 6D). In both ZAR1 and NRCs, activation
521 triggers the formation of pentameric or hexameric resistosomes, which initiate the
522 downstream hypersensitive response (11, 22, 35). However, it is still unclear whether R2
523 forms a resistosome similar to those of NRCs or ZAR1 and induces cell death through a
524 comparable mechanism. Notably, R2 contains the MADA motif, which is critical for cell death
525 initiation in many NLRs. In contrast, the EDVID motif—a conserved feature found in ZAR1,
526 Sr35, NRCs, and many other NLRs—is absent in R2 (Fig. S13) (26, 37, 38). The presence
527 and absence of MADA and EDVID motifs, and the necessity of the hydrophobic core
528 described here, suggest that different types of CC-NLRs may have unique structural and
529 sequence features within their CC domains, resulting in distinct regulatory mechanisms.

530

531 **Material and Methods**

532

533 Plant material and growth conditions

534 Wild-type and *nrc2/3/4_KO N. benthamiana* plants were grown in a walk-in growth chamber
535 maintained at 25 °C, under a 16 h light/8 h dark cycle. (39).

536

537 Plasmid construction

538 The CC, NB-ARC, and LRR domains of NRC2/4 were modularized and cloned into the
539 Golden Gate Level 0 acceptor vector pAGM9121 (40). Site-directed mutagenesis were
540 performed on the CC domain Level 0 module using inverse PCR, and then digested with
541 AarI (NEB) and ligated with T4 DNA ligase (Thermo Scientific). The mutated CC domain
542 modules were assembled with the NB-ARC and LRR modules, along with a C-terminal 4x
543 Myc tag or GFP tag, into the pICH86988 binary vector, containing the 35S promoter and
544 OCS terminator, using Golden Gate assembly (40, 41). The pICH86988 constructs
545 containing NRC4-myc or GFP were subsequently transformed into *Agrobacterium*
546 *tumefaciens* strain GV3101(pMP90). For in vitro translation experiments, the CC domain
547 module of NRC4 (wild-type and hydrophobic core mutants) was assembled with the T7
548 promoter, CMV1 5' UTR, T7 terminator, and an overhang-modified C-terminal Myc tag
549 (CTCA-GCTT) into the acceptor vector pICSL86900OD (41). To study the hydrophobic core

550 function in R2, Rx, Bs2, Rpi-amr1, and Rpi-amr3, the CDS of Rpi-amr1 and Rpi-amr3 were
551 cloned into Level 0 acceptor pAGM9121 and CDS of R2, Bs2, and Rx contained the
552 overhang and BsaI cutting site were cloned into pTA vector (42–45). For NbZAR1, an D481V
553 mutation variant (autoactive) Level 0 plasmid was used (46). Site-directed mutagenesis in
554 the CC domain was performed as described above. The resulting NLRs variants were
555 subcloned into pICH86988 for cell death assays. The effector genes AVR2 and AVRamr3
556 were synthesized and assembled into pICH47751 and pICH47761 vectors, incorporating the
557 35S promoter and OCS terminator (43, 47). The primers used for cloning and the plasmids
558 used in this study are listed in Datasets S1 and S2 .
559
560 Agroinfiltration
561 *A. tumefaciens* GV3101(pMP90) was used to express NLRs and effectors. The
562 *Agrobacterium* stocks were refreshed on 523 medium containing the appropriate antibiotics
563 and incubated overnight at 28°C. The cells were harvested by centrifugation at 5000 × g for
564 5 minutes and resuspended in MMA buffer (10 mM $MgCl_2$, 10 mM MES-KOH, 150 μM
565 acetosyringone, pH 5.6). The cell concentrations were adjusted to 0.2 for all NLRs and 0.1
566 for all effectors for subsequent experiments. *Agrobacterium* suspensions with the desired
567 optical density (OD) were infiltrated into *N. benthamiana* leaves using a 1 mL syringe.
568
569 Cell death assay
570 The complementation assays were performed in the *nrc2/3/4*_KO *N. benthamiana*, while
571 functional analyses of hydrophobic core-mutated R2, NbZAR1, Rx, Bs2, Rpi-amr1, and Rpi-
572 amr3 were conducted in wild-type *N. benthamiana*. The NLR proteins and their
573 corresponding effectors were transiently expressed in *N. benthamiana* using *A. tumefaciens*
574 strains carrying expression vectors for the indicated proteins. Cell death intensity was
575 quantified using the UVP ChemStudio Imaging System (Analytik Jena) at 6 dpi for NRC4
576 mutant screen and at 3 dpi for R2, NbZAR1, Rx, Bs2, Rpi-amr1, and Rpi-amr3 mutants.
577 Autofluorescence of necrotic regions was detected using the blue LED excitation light and a
578 FITC emission filter (519 nm). Cell death intensity was normalized by dividing the pixel value
579 by the maximum signal pixel value (65535) detected by the UVP ChemStudio.
580
581 Protein extraction for SDS-PAGE analysis
582 The protein extraction method was conducted as previously described (48). The leaf disc
583 was homogenized with ceramic beads in a tissue homogenizer under liquid nitrogen. Total
584 protein was extracted with GTEN buffer comprising 10% glycerol, 25 mM Tris (pH 7.5), 1
585 mM EDTA, 150 mM NaCl, 2% (w/v) PVPP, 10 mM DTT, 1× protease inhibitor cocktail
586 (Sigma, P9599), and 0.2% IGEPAL (Sigma). The protein extract was centrifuged at 5000 ×g

587 for 10 minutes at 4 ℃, and the supernatant was transferred to a new Eppendorf tube and
588 centrifuged again at 13000 ×g for 5 minutes at 4 ℃ to remove the remaining debris as much
589 as possible. The final supernatant was combined with 4x sample loading dye containing 200
590 mM Tris-HCl (pH 6.8), 8% (w/v) SDS, 40% (v/v) glycerol, 50 mM EDTA, 0.08% bromophenol
591 blue, and 0.1 M DTT. The protein samples were incubated at 70 ℃ for 10 minutes before
592 SDS-PAGE analysis.
593
594 SDS-PAGE assay and immunodetection analysis
595 SDS-PAGE electrophoresis and immunodetection analyses were conducted as previously
596 described (48). Denatured samples were separated on PAGE gels prepared with 10% or
597 15% T-Pro EZ gel solution (Omics bio), containing 0.1% TEMED (Bio-Rad) and 0.1%
598 ammonium persulfate (Bio-Rad). Proteins were transferred to a PVDF membrane using the
599 Trans-Blot Turbo Transfer System (Bio-Rad). Following the transfer, the membrane was
600 washed with Tris buffer saline (TBS) with 0.1% Tween-20 and blocked with 5% nonfat dry
601 milk. For immunodetection, anti-Myc (GenScript, A00704) and anti-H+ATPase (Agrisera,
602 AS07 260) were used as primary antibodies for NRC4 protein and membrane fraction
603 detection, respectively. Secondary antibodies included Peroxidase AffiniPure Goat Anti-
604 Mouse IgG (H+L) (Jackson, 115-035-003) and Peroxidase Conjugated Goat Anti-Rabbit IgG
605 (H+L) (Sigma, AP132P). Primary antibodies were diluted at 1:5000, and the secondary
606 antibodies were diluted at 1:20000. Chemiluminescence signals were detected using a
607 mixture of SuperSignal West Pico PLUS Chemiluminescent Substrate (Thermo Scientific,
608 34580) and SuperSignal West Femto Maximum Sensitivity Substrate (Thermo Scientific,
609 34096) in a 3:1 ratio. Images were captured using the UVP ChemStudio Imaging System.
610 SimplyBlue SafeStain (Invitrogen, 465034) was used to visualize the rubisco signal on the
611 PVDF membrane.
612
613 Blue Native PAGE
614 The BN-PAGE method was conducted as previously described (35). To assess whether
615 oligomerization was affected in the mutants, we transiently expressed the NRC4
616 hydrophobic core mutants along with Rpi-blb2, with or without AVRblb2, in 4-week-old
617 plants. Leaf discs were collected at 2 and 3 dpi, and total protein was extracted using a
618 native PAGE extraction buffer containing 50 mM HEPES (pH 7.5), 50 mM NaCl, 5 mM
619 MgCl2, 10% glycerol, 10 mM DTT, 1x protease inhibitor cocktail (Sigma, P9599), and 1%
620 digitonin (Sigma, D141). Protein extracts were incubated on ice at 4℃ for 10 minutes,
621 followed by centrifugation at 12,000 rpm for 15 minutes at 4℃. The supernatant was
622 transferred to a new tube and centrifuged again at 12,000 rpm for 10 minutes at 4℃ to avoid

623 the interference of the pellet. The resulting protein extracts were diluted to 0.4x using the
624 native PAGE extraction buffer. Diluted samples were then mixed with 4x sample buffer and
625 NativePAGE™ 5% G-250 Sample Additive to achieve a final G-250 concentration of
626 0.125%. Samples were loaded onto a 4–16% Native PAGE gel (Invitrogen, BN1002) and
627 electrophoresis was carried out following the manufacturer's protocol. In brief, Native PAGE
628 was performed using the XCell system (Invitrogen) under 4℃. The gel was run with a dark
629 cathode buffer at 150 V for 45 minutes, followed by replacing the dark cathode buffer with a
630 light cathode buffer and continuing at 200 V for 120 minutes. After electrophoresis, proteins
631 were transferred to a PVDF membrane using the Trans-Blot Turbo Transfer System (Bio-
632 Rad). The membrane was fixed with 8% acetic acid, air-dried in a chemical hood, and
633 subsequently rinse with 99% ethanol. The membrane was washed with ddH_2O and TBST to
634 remove residual ethanol before the immunodetection mentioned above.
635
636 <u>In vitro translation</u>
637 The plasmid containing the *T7-CMV1:NRC4 CC-Myc* fragmentwas amplified using the T7
638 promoter forward primer and the T7 terminator reverse primer with the KAPA HiFi HotStart
639 ReadyMix (Roche). The resulting PCR fragments were purified using a FavorPrep GEL/PCR
640 purification Mini kit (Favorgen). The in vitro translation assay was performed following the
641 protocol of the TNT-T7 coupled wheat germ extract system (Promega). Briefly, 1 µg purified
642 PCR fragments were mixed with the TNT wheat germ extract, TNT reaction buffer, amino
643 acid mixture, RNase inhibitor, and T7 polymerase. The reaction mixture was incubated at 30
644 ℃ for 2 hours. The NRC4-CC domain tagged with 4× Myc was subsequently analyzed by
645 immunoblotting mentioned above.
646
647 <u>Lipid binding assay</u>
648 The PIP strips (Invitrogen) were first blocked by incubating with 3% bovine serum albumin
649 (Fraction V, low heavy metal, MERK) at room temperature for one hour. The NRC4 CC
650 domain proteins, obtained from in vitro translation, were then incubated with the PIP strips at
651 4°C overnight. Following incubation, the PIP strips were washed with TBST before the
652 immunodetection assay as described above.
653
654 <u>Protein fractionation</u>

655 Membrane enrichment was performed using a slightly modified version of a previously
656 described protocol (49). NRC4 was transiently co-expressed with *Rpi-blb2*, with or without
657 *AVRblb2*, in *nrc2/3/4_KO N. benthamiana*. At 2 dpi, leaves were harvested and
658 homogenized under liquid nitrogen using a pestle and mortar. The powdered leaf tissue was

659 mixed with membrane protein extraction buffer (0.33 M sucrose, 20 mM Tris-HCl [pH 8], 1
660 mM EDTA), supplemented with 5 mM DTT, 1× protease inhibitor (Thermo Scientific), and
661 0.5% PVPP. The mixture was first centrifuged at 2000 ×g, and the supernatants were further
662 filtering through Miracloth (MERK, 475855-1R). The supernatant was transferred to a new
663 Eppendorf tube, and 50 µl was set aside as the total protein fraction. The remaining
664 supernatant was ultracentrifuged at 21,000 ×g for 1.5 hours to separate the soluble protein
665 fraction and the membrane protein. The soluble protein fraction was transferred to a new
666 Eppendorf tube, while the pellet was resuspended in a membrane extraction buffer (without
667 PVPP) at one-third the volume of the soluble protein fraction. The membrane fraction was
668 then diluted threefold with a membrane extraction buffer (without PVPP) before being
669 applied to SDS-PAGE and immunoblotting analysis.

670 Confocal microscopy

671 To analyze the subcellular localization of wild-type and hydrophobic core-mutated NRC4,
672 four-week-old *nrc2/3/4_KO N. benthamiana* plants were agroinfiltrated with NRC4-GFP, HF-
673 Rpi-blb2, mTagBFP, NbSOBIR1-mCherry, and either with or without Flag-AVRblb2. At 2 or 3
674 days post-infiltration (dpi), discs of the infiltrated leaves were imaged using an Andor
675 Dragonfly spinning disc confocal microscope (Andor) equipped with a 40× water immersion
676 objective lens (Advanced optical microscope core facility, Academia Sinica) or Leica Stellaris
677 8 inverted confocal microscope with 40x water immersion objective lens (Live-cell-image
678 core lab, Institute of Plant and Microbiology, Academia Sinica). Excitation wavelengths of
679 405 nm, 488 nm, and 561 nm were used for BFP, GFP, and mCherry, respectively. The
680 corresponding emission wavelengths were 422–468 nm for BFP, 505–550 nm for GFP, and
681 572–615 nm for mCherry. Chloroplast autofluorescence was labeled using excitation at 637
682 nm and emission in the range of 660–737 nm. For imaging of NRC4 haustoria accumulation,
683 *P. infestans* inoculation was performed as described below. After 1 day of inoculation, leaf
684 discs from the infected regions were imaged using a 40x water immersion objective lens on
685 a Leica Stellaris 8 inverted confocal microscope. The single-plane images were exported to
686 Fiji (ImageJ) software for quantitative analysis. GFP and RFP signals were measured at
687 selected areas (5 µm) spanning the peripheral cytoplasm and across the extrahaustorial
688 membrane (EHM).
689

690 Inoculation of *Phytothroa infestans*

691 *P. infestans* 214009 (a gift from Dr. Jin-Hsing Huang, Taiwan Agriculture Research Institute)
692 was originally isolated from Taiping, Taichung City, Taiwan. *P. infestans* was maintained on
693 Rye sucrose medium at 19°C under dark conditions. Before performing the focal
694 accumulation assay for NRC4, *P. infestans* was subcultured on detached *N. benthamiana*

695 leaves. For the EHM focal accumulation assay, leaves from 4-week-old *nrc2/3/4*_KO *N.*
696 *benthamiana* plants were infiltrated with *Agrobacterium* containing either wild-type or
697 hydrophobic core mutant NRC4 constructs and a cytosolic RFP marker. Zoospores were
698 collected from sporangia on *P. infestans*-infected *N. benthamiana* leaves by incubating the
699 sporangia in sterile water at 4°C. The zoospores were then inoculated onto detached *N.*
700 *benthamiana* leaves at 2 days after transient expression of NRC4 variants.
701
702 Protein structure prediction
703 To identify the position n of the conserved hydrophobic residue candidates, we applied
704 AlphaFold 3 to predict the NRC4 monomer (pTM=0.82) (50). Assuming similar protein
705 conformation, we superimposed the NRC4 monomer to the published NbNRC2 dimer (PDB:
706 8RFH) by using the "Matchmaker" function to further correct the NbNRC4 structure we
707 obtained from AlphaFold3 (50). Since the CC domain is missing in this NbNRC2 homodimer
708 structure and may make the CC domain differ from the current model, we cross compared
709 the position of the hydrophobic core on the NbNRC4 resistosome structure (PDB: 9CC8).
710
711 Phylogenetic analysis

712 The amino acid sequences of NB-ARC domain of the NRC superfamily from 20 species
713 representing various genera within the Solanaceae were extracted from the dataset in the
714 NLRdome (36). A total of 2,581 sequences, including reference NLR sequences, were
715 aligned using MAFFT (51). Gaps in the aligned sequences were manually removed, and the
716 trimmed amino acid sequences were used for phylogenetic analysis in MEGA (Molecular
717 Evolutionary Genetics Analysis) (52). The phylogenetic analysis employed the Maximum
718 Likelihood method with the JTT+G+I evolutionary model and 500 bootstrap tests to assess
719 the reliability of the tree. NLR clades were further categorized based on the grouping criteria
720 outlined in the previous study (53).

721
722 Hydrophobic core amino acid logo creation and entropy analysis

723 The full-length NLR amino acid sequences and the CC domain sequences from each clade
724 were extracted and aligned using MAFFT, with NRC2/3/4 serving as the reference for
725 identifying the hydrophobic core. To create the amino acid logo, the corresponding residues
726 of the hydrophobic core in each clade were extracted, and the reference NRC2/3/4
727 sequences were removed. Amino acid logos for each clade were then generated based on
728 the extracted hydrophobic core residues using WebLogo 3
729 (https://weblogo.threeplusone.com/create.cgi) (54). After CC domain alignment and removal

730 of NRC2/3/4 sequences, the remaining sequences were subjected to entropy analysis.
731 Shannon entropy was calculated using an online tool developed by the Los Alamos National
732 Laboratory (https://www.hiv.lanl.gov/content/sequence/ENTROPY/entropy.html). The
733 hydrophobic core was labeled and a cutoff score of 0.75 was applied to identify highly
734 variable residues compared to the NRC group. Detailed analysis results are included in the
735 Dataset S3.

736

737 **Acknowledgments**

738 We thank Mark Youles (SynBio, The Sainsbury Laboratory, UK) for sharing plasmids for
739 molecular cloning. We thank Mei-Jane Fang and Ji-Ying Huang in the Live-Cell-Imaging
740 Core Lab (Institute of Plant and Microbial Biology, Academia Sinica, Taiwan), and Shu-Chen
741 Shen in the Advanced Optical Microscope Core Facility (Agricultural Biotechnology
742 Research Center, Academia Sinica, Taiwan) for help with confocal imaging. We thank Dr.
743 Jin-Hsing Huang (Taiwan Agriculture Research Institute) for providing the *P. infestans*
744 isolated 214009 and advice on pathogen inoculation. This project was funded by the 2030
745 Emerging Young Scholar Program of the National Science and Technology Council (NSTC)
746 of Taiwan (NSTC-112-2628-B-001-007), a bilateral exchange grant of NSTC and Royal
747 Society (UK) (NSTC-113-2927-I-001-514, IEC\NSFC\233289), and the intramural fund of
748 Institute of Plant and Microbial Biology, Academia Sinica, Taiwan.

749

750 **Author Contributions**

751 HYW and CHW contributed to the conceptualization of the project. HYW and FJG
752 contributed to data curation. HYW and CHW contributed to the formal analysis. HWY and
753 CHW contributed to the investigation. KTL and FJG contributed to the methodology. TOB
754 and CHW supervised the research and acquired funding. CHW managed the project. HYW
755 contributed to data visualization. HYW and CHW wrote the initial manuscript draft. HYW and
756 CHW edited the manuscript.

757 **Data Availability**

758 All study data are included in the article and/or supporting information.

759 **Competing Interest Statement**

760 TOB receives funding from the industry and co-founded a start-up company (Resurrect Bio
761 Ltd.) on NLR biology.

762 **Supporting Information**

763 **Figure S1.** Alignment of CC domain of NbNRC2/3/4 and AtZAR1.
764
765 **Figure S2.** The protein accumulation of NRC4 hydrophobic residues mutant variants.
766
767 **Figure S3.** The localization of the hydrophobic center in the resting state NRC4 and the
768 activated state R-cluster.
769
770 **Figure S4.** The hydrophobic center of CC domain in the resting and activated state of
771 NRC2.
772
773 **Figure S5.** $NRC4^{AAA}$ showed no cell death in 2 dpi compared to wild-type NRC4**.**
774
775 **Figure S6.** Mutations on the hydrophobic core do not affect NRC4 subcellular localization in
776 the resting state.
777
778 **Figure S7.** The mutation on A72 delays the formation of the resistosome and punctates on
779 the plasma membrane.
780
781 **Figure S8.** Mutations of hydrophobic residues outside the hydrophobic core did not affect
782 the association of the NRC4 CC domain with phospholipids.
783
784 **Figure S9.** Mutations of the hydrophobic core do not affect the NRC4 focal accumulation on
785 the EHM.
786
787 **Figure S10.** Phylogenetic tree of NRC superclade in representative solanaceous plant.
788
789 **Figure S11.** Quantitative cell death result of NRC2, NRC3, R2, and NbZAR1 variants.
790
791 **Figure S12.** Quantitative cell death result of the representative Rx, Bs2, Rpi-amr1, and Rpi-
792 amr3.
793
794 **Figure S13.** The EDVID motif is absent in R2.
795
796 **Table S1.** List of the constructs used in cell death assays.
797
798 **Table S2.** List of the constructs used in lipid binding assays.
799
800 **Table S3.** List of the constructs used in cell biology assays.
801
802 **Table S4.** List of the constructs used in BN-PAGE assays.
803
804 **Table S5.** List of the constructs used in cell fractionation assays.
805
806 **Table S6.** List of the constructs used in focal assays.
807
808 **Dataset S1.** List of primers used in this study. (XLSX)

809 **Dataset S2.** List of plasmids used in this study. (XLSX)

Dataset S3. Results of entropy analysis. (XLSX)

File S1. NRC superfamily phylogenetic tree files of 22 species.

File S2. Amino acid sequences of CC domain of NRC superfamily for entropy analysis.

References

1. J. D. G. Jones, J. L. Dangl, The plant immune system. *Nature* **444**, 323–329 (2006).
2. B. P. M. Ngou, H.-K. Ahn, P. Ding, J. D. G. Jones, Mutual potentiation of plant immunity by cell-surface and intracellular receptors. *Nature* **592**, 110–115 (2021).
3. J. D. G. Jones, B. J. Staskawicz, J. L. Dangl, The plant immune system: From discovery to deployment. *Cell* **187**, 2095–2116 (2024).
4. Z. Duxbury, C. Wu, P. Ding, A Comparative Overview of the Intracellular Guardians of Plants and Animals: NLRs in Innate Immunity and Beyond. *Annual Review of Plant Biology* **72**, 155–184 (2021).
5. S. Ma, *et al.*, Direct pathogen-induced assembly of an NLR immune receptor complex to form a holoenzyme. *Science* **370**, eabe3069 (2020).
6. R. Martin, *et al.*, Structure of the activated ROQ1 resistosome directly recognizing the pathogen effector XopQ. *Science* **370**, eabd9993 (2020).
7. S. Huang, *et al.*, Identification and receptor mechanism of TIR-catalyzed small molecules in plant immunity. *Science* **377**, eabq3297 (2022).
8. A. Jia, *et al.*, TIR-catalyzed ADP-ribosylation reactions produce signaling molecules for plant immunity. *Science* **377**, eabq8180 (2022).
9. H. Yu, *et al.*, Activation of a helper NLR by plant and bacterial TIR immune signaling. *Science* **386**, 1413–1420 (2024).
10. L. Wan, *et al.*, TIR domains of plant immune receptors are NAD+-cleaving enzymes that promote cell death. *Science* **365**, 799–803 (2019).
11. J. Wang, *et al.*, Reconstitution and structure of a plant NLR resistosome conferring immunity. *Science* **364**, eaav5870 (2019).
12. G. Bi, *et al.*, The ZAR1 resistosome is a calcium-permeable channel triggering plant immune signaling. *Cell* **184**, 3528-3541.e12 (2021).
13. P. Jacob, *et al.*, Plant “helper” immune receptors are Ca2+-permeable nonselective cation channels. *Science* **373**, 420–425 (2021).
14. S. C. Saile, *et al.*, Arabidopsis ADR1 helper NLR immune receptors localize and function at the plasma membrane in a phospholipid dependent manner. *New Phytologist* **232**, 2440–2456 (2021).
15. Z. Wang, *et al.*, Plasma membrane association and resistosome formation of plant helper immune receptors. *Proceedings of the National Academy of Sciences* **120**, e2222036120 (2023).
16. M. P. Contreras, D. Lüdke, H. Pai, A. Toghani, S. Kamoun, NLR receptors in plant immunity: making sense of the alphabet soup. *EMBO reports* **24**, e57495 (2023).
17. C.-H. Wu, *et al.*, NLR network mediates immunity to diverse plant pathogens. *Proceedings of the National Academy of Sciences* **114**, 8113–8118 (2017).
18. C.-H. Wu, L. Derevnina, S. Kamoun, Receptor networks underpin plant immunity. *Science* **360**, 1300–1301 (2018).
19. H. Adachi, L. Derevnina, S. Kamoun, NLR singletons, pairs, and networks: evolution, assembly, and regulation of the intracellular immunoreceptor circuitry of plants. *Curr Opin Plant Biol* **50**, 121–131 (2019).
20. F.-J. Goh, C.-Y. Huang, L. Derevnina, C.-H. Wu, NRC Immune receptor networks show

858 diversified hierarchical genetic architecture across plant lineages. *The Plant Cell* **36**,
859 3399–3418 (2024).
860 21. T. Sakai, *et al.*, The NRC0 gene cluster of sensor and helper NLR immune receptors is
861 functionally conserved across asterid plants. *The Plant Cell* **36**, 3344–3361 (2024).
862 22. F. Liu, *et al.*, Activation of the helper NRC4 immune receptor forms a hexameric
863 resistosome. *Cell* **187**, 4877-4889.e15 (2024).
864 23. J. Madhuprakash, *et al.*, A disease resistance protein triggers oligomerization of its
865 NLR helper into a hexameric resistosome to mediate innate immunity. *Science*
866 *Advances* **10**, eadr2594 (2024).
867 24. S. Ma, *et al.*, Oligomerization-mediated autoinhibition and cofactor binding of a plant
868 NLR. *Nature* **632**, 869–876 (2024).
869 25. M. Selvaraj, *et al.*, Activation of plant immunity through conversion of a helper NLR
870 homodimer into a resistosome. *PLOS Biology* **22**, e3002868 (2024).
871 26. A. Förderer, *et al.*, A wheat resistosome defines common principles of immune receptor
872 channels. *Nature* **610**, 532–539 (2022).
873 27. S. Wang, *et al.*, Delivery of cytoplasmic and apoplastic effectors from Phytophthora
874 infestans haustoria by distinct secretion pathways. *New Phytologist* **216**, 205–215
875 (2017).
876 28. T. O. Bozkurt, S. Kamoun, The plant–pathogen haustorial interface at a glance. *Journal*
877 *of Cell Science* **133**, jcs237958 (2020).
878 29. T. O. Bozkurt, *et al.*, Rerouting of plant late endocytic trafficking toward a pathogen
879 interface. *Traffic* **16**, 204–226 (2015).
880 30. T. O. Bozkurt, *et al.*, Phytophthora infestans effector AVRblb2 prevents secretion of a
881 plant immune protease at the haustorial interface. *Proceedings of the National*
882 *Academy of Sciences* **108**, 20832–20837 (2011).
883 31. S. Wang, *et al.*, Phytophthora infestans RXLR effectors act in concert at diverse
884 subcellular locations to enhance host colonization. *Journal of Experimental Botany* **70**,
885 343–356 (2019).
886 32. C. Duggan, *et al.*, Dynamic localization of a helper NLR at the plant–pathogen interface
887 underpins pathogen recognition. *Proc. Natl. Acad. Sci. U.S.A.* **118**, e2104997118
888 (2021).
889 33. J. Rausche, *et al.*, A phosphoinositide 5-phosphatase from Solanum tuberosum is
890 activated by PAMP-treatment and may antagonize phosphatidylinositol 4,5-
891 bisphosphate at Phytophthora infestans infection sites. *New Phytologist* **229**, 469–487
892 (2021).
893 34. H. Adachi, *et al.*, An N-terminal motif in NLR immune receptors is functionally
894 conserved across distantly related plant species. *eLife* **8**, e49956 (2019).
895 35. M. P. Contreras, *et al.*, Sensor NLR immune proteins activate oligomerization of their
896 NRC helpers in response to plant pathogens. *The EMBO Journal* **42**, e111519 (2023).
897 36. Y. Sugihara, A. Toghani, S. Kamoun, J. Kourelis, NLRome dataset from 124 genomes
898 of plants in the Solanaceae family. Zenodo. https://doi.org/10.5281/zenodo.10354350.
899 Deposited 12 December 2023.
900 37. G. J. Rairdan, *et al.*, The Coiled-Coil and Nucleotide Binding Domains of the Potato Rx
901 Disease Resistance Protein Function in Pathogen Recognition and Signaling. *The Plant*
902 *Cell* **20**, 739–751 (2008).
903 38. T. Wróblewski, *et al.*, Genome-wide functional analyses of plant coiled–coil NLR-type
904 pathogen receptors reveal essential roles of their N-terminal domain in oligomerization,
905 networking, and immunity. *PLOS Biology* **16**, e2005821 (2018).
906 39. C.-H. Wu, *et al.*, NRC4 Gene Cluster Is Not Essential for Bacterial Flagellin-Triggered
907 Immunity1. *Plant Physiology* **182**, 455–459 (2020).
908 40. E. Weber, C. Engler, R. Gruetzner, S. Werner, S. Marillonnet, A modular cloning
909 system for standardized assembly of multigene constructs. *PLoS One* **6**, e16765
910 (2011).
911 41. C. Engler, *et al.*, A Golden Gate Modular Cloning Toolbox for Plants. *ACS Synth. Biol.*
912 **3**, 839–843 (2014).

42. T. H. Tai, *et al.*, Expression of the Bs2 pepper gene confers resistance to bacterial spot disease in tomato. *Proceedings of the National Academy of Sciences* **96**, 14153–14158 (1999).
43. E. M. Gilroy, *et al.*, Involvement of cathepsin B in the plant disease resistance hypersensitive response. *The Plant Journal* **52**, 1–13 (2007).
44. K. Witek, *et al.*, Accelerated cloning of a potato late blight–resistance gene using RenSeq and SMRT sequencing. *Nat Biotechnol* **34**, 656–660 (2016).
45. K. Witek, *et al.*, A complex resistance locus in Solanum americanum recognizes a conserved Phytophthora effector. *Nat. Plants* **7**, 198–208 (2021).
46. M. P. Contreras, *et al.*, The nucleotide-binding domain of NRC-dependent disease resistance proteins is sufficient to activate downstream helper NLR oligomerization and immune signaling. *New Phytologist* **243**, 345–361 (2024).
47. X. Lin, *et al.*, A potato late blight resistance gene protects against multiple *Phytophthora* species by recognizing a broadly conserved RXLR-WY effector. *Molecular Plant* **15**, 1457–1469 (2022).
48. J. Win, S. Kamoun, A. M. E. Jones, “Purification of Effector–Target Protein Complexes via Transient Expression in Nicotiana benthamiana” in *Plant Immunity: Methods and Protocols*, J. M. McDowell, Ed. (Humana Press, 2011), pp. 181–194.
49. L. Abas, C. Luschnig, Maximum yields of microsomal-type membranes from small amounts of plant material without requiring ultracentrifugation. *Analytical Biochemistry* **401**, 217–227 (2010).
50. J. Abramson, *et al.*, Accurate structure prediction of biomolecular interactions with AlphaFold 3. *Nature* **630**, 493–500 (2024).
51. K. Katoh, J. Rozewicki, K. D. Yamada, MAFFT online service: multiple sequence alignment, interactive sequence choice and visualization. *Briefings in Bioinformatics* **20**, 1160–1166 (2019).
52. S. Kumar, G. Stecher, K. Tamura, MEGA7: Molecular Evolutionary Genetics Analysis Version 7.0 for Bigger Datasets. *Molecular Biology and Evolution* **33**, 1870–1874 (2016).
53. K. Seong, E. Seo, K. Witek, M. Li, B. Staskawicz, Evolution of NLR resistance genes with noncanonical N-terminal domains in wild tomato species. *New Phytologist* **227**, 1530–1543 (2020).
54. G. E. Crooks, G. Hon, J.-M. Chandonia, S. E. Brenner, WebLogo: A Sequence Logo Generator. *Genome Res.* **14**, 1188–1190 (2004).